Temperature-induced crystallinity and vibrational properties in samarium orthovanadate

Emin Varghese,[1,*] Sourabh Kumar,[2,*] Biswarup Pathak,[1,2] and Somaditya Sen[1,3,4,†]

[1]*Discipline of Metallurgy and Materials Science, School of Basic Sciences Indian Institute of Technology (IIT) Indore, Indore, Madhya Pradesh 453552, India*

[2]*Discipline of Chemistry, School of Basic Sciences, School of Basic Sciences Indian Institute of Technology (IIT) Indore, Indore, Madhya Pradesh 453552, India*

[3]*Discipline of Physics, School of Basic Sciences Indian Institute of Technology (IIT) Indore, Indore, Madhya Pradesh 453552, India*

[4]*Electronics Engineering, Ming-Chi University of Technology, New Taipei, Taiwan*

(Received 8 February 2020; revised manuscript received 23 March 2020; accepted 2 April 2020; published 21 May 2020)

The Samarium orthovanadates particles were prepared using the sol-gel method, and the effect of sintering temperature on the crystallinity was studied in detail through x-ray diffraction (XRD) and the Rietveld refinement of the obtained XRD data. Density functional theory (DFT) based calculations were used to describe the dynamic properties in Samarium orthovanadate. The data obtained from the DFT calculations were made instrumental in confirming the vibrational properties, and both the Raman and infrared modes obtained through the experiments. Temperature-dependent Raman spectroscopy was used to provide a deeper insight into all the eigenmodes and their behavior with varying temperature. A temperature-dependent (experiment) and pressure-dependent (DFT) Raman spectra were produced for the investigation of eigenmodes in the samples. A correlation between the two methods was seen, and the alignment between the two data sets was found to be ineluctable. The Grüneisen parameter of individual modes were calculated with the aid of the theoretically obtained variation in the Raman shift with respect to the bulk modulus. Ultraviolet-visible spectroscopy of the samples was explored to study possible correlation with temperature, and theoretical bandgaps were obtained through standard DFT and hybrid exchange-correlation functional calculations. Photoluminescence spectroscopy was performed in the hopes of unveiling possible applications of the material.

DOI: 10.1103/PhysRevB.101.174112

I. INTRODUCTION

Human curiosity has led to many discoveries and inventions, which have led to ever-rising technological growth. Finding an efficient and better way to get results has been the quest of mankind from the beginning. The use of materials that serve a purpose more efficiently would undoubtedly be pursued after over a less efficient counterpart. The advent of research in the field of materials science could be attributed to this ever prevalent quest. Orthovanadates are a peculiar type of compound because of the unique crystal structures that are observed. Altering the size of the *A*-site atom has shown that orthovanadates can assume both monoclinic and tetragonal forms in normal conditions. An irreversible tetragonal zircon (space group: $I4_1/amd$) to tetragonal scheelite (space group: $I4_1/a$) phase transition is observed in the case of zircon type compounds with small-sized cations [1–3]. These are comprised of $HoVO_4$, $EuVO_4$, $TbVO_4$, $SmVO_4$, and $LuVO_4$ at pressures of 6−8 GPa. Another reversible scheelite to fergusonite (space group: $I4_1/a$) transition is observed at higher pressures. $NdVO_4$ at 18.1 GPa and $CeVO_4$ at 14.7 GPa show a second reversible transition from the fergusonite to an orthorhombic phase [4,5]. This property, coupled with its unique electronic structure, makes them a fascinating class of materials. Orthovanadates have been found to have considerable use in various fields. Lanthanide orthovanadates are indispensable as catalysts, polarizers, solid-state protonic conductors, phosphors, and low threshold laser hosts. These materials illustrate attractive magnetic, thermally activated, optical, and x-ray luminescent properties. Considerable research has been performed on lanthanum orthovanadate, $LaVO_4$, attributed to its surface catalytic properties. $LaVO_4$ exist in monoclinic monazite crystal structure under normal circumstances, which is in contrast with the rest of the rare-earth orthovanadates that exist in a zircon state. The coordination number of Ln^{3+} is "8" in the tetragonal zircon structure and "9" in the monoclinic monazite structure. This aberration in the crystal structure of $LaVO_4$ is attributed to the larger size of La^{3+} compared to the rest of the rare-earth ions. This is due to the lower effective charge (leading to less electrostatic force on the surrounding electrons) and less efficient shielding by *f*-shell electrons in the case of the remaining rare-earth elements (Lanthanide contraction). Samarium orthovanadate, $SmVO_4$, exists in the tetragonal zircon phase (space group: $I4_1/amd$) under ambient conditions. Like other rare-earth orthovanadates, $SmVO_4$ has been a material of intrigue from the various applications it has, from being used as catalysts [6], optical polarizers [7], solar cells [8] to gas sensors [9], and thin-film phosphors [10]. The effect of pressure and the accompanying metastable phase transformation of $SmVO_4$

*These authors have contributed equally to this work.
†sens@iiti.ac.in

has been studied [6]. A study on the pressure-induced phase transformation in zircon-type orthovanadate $SmVO_4$ from experiment and theory has been conducted in the recent past [11]. Alternate routes for the synthesis of $SmVO_4$ via hydrothermal method mediated by a chelating ligand using decavanadate as the source of vanadium have also been studied [12].

The theoretical approach has rarely been employed in RVO_4 compounds. Density functional theory (DFT) is widely used for first-principles studies of crystalline materials. DFT provides considerable insight into the lattice dynamics of the compounds. In $SmVO_4$, the phase obtained at ambient and the temperatures explored in this study are stable at $T \sim 0$ K; hence the issue of stabilizing the phase is not a concern, and the DFT studies can be used to analyze the experimental data in detail. This work is focused on intertwining the experimental data obtained from the experiments performed, and the theoretical calculations performed using DFT, including the phonon modes, phonon lifetimes, and the band-gap variation with temperature. The infrared (IR) and Raman spectroscopy are used to study the crystallinity collectively with the DFT methods. An image can be generated, which would further enhance the idea derived. A temperature-induced crystallinity is linked with the vibrational properties of $SmVO_4$, with several experimental measurements and theoretical explanations.

Experimental section

$SmVO_4$ (hereafter called SV) samples were prepared via the sol-gel method using samarium (III) oxide (Sm_2O_3 of purity 99.9%), and vanadium (V) oxide (V_2O_5 of purity 99.99%) from Alfa Aesar. The oxides were individually dissolved in calculated quantities of dilute HNO_3. The solutions were added to each other and stirred for 2 h for homogeneous mixing to form the precursor solution. In a separate solution, a mixture of citric acid and ethylene glycol was prepared. When heated, this mixture first forms monomers, which on further heating chain up to form polymers. This polymeric solution initially serves as a gelling agent. The precursor solution was added to this polymeric solution, which allows the precursor ions to get attached to the polymeric chains and restore the homogeneity of the ions. Heating at a temperature of about $\sim 50\,^{\circ}$C ensures the homogeneous attachment of the precursor ions to the polymer chains. On dehydration of this polymeric solution, gelling happens. With further heating, the polymeric chains start to break down, providing the much-needed energy to form chemical bonds between the homogeneously distributed ions, thus achieving excellent chemical homogeneity of the desired formula. The gels were burnt in ambiance to form black powders. During this process, nitrogenous and carbonaceous oxides were liberated. However, the burnt black powders still contained nitrogenous and carbonaceous components to remove which they were heated at 450°C (723 K) for 6 h. These samples were finely ground and sintered at 600 °C (873 K). This powder is named SV1 from now on. SV1 was reground, and further sintered at 750 °C (1023 K). The resultant powder was named SV2. Another cycle of grinding and heating of the SV2 powders, this time at 900 °C (1173 K), yielded SV3 powders. The process is economical and straightforward and requires simple processing equipment [13,14]. X-ray diffraction (XRD) patterns were obtained using a Bruker D2 Phaser diffractometer (in the range, $2\theta = 10^{\circ}$ to 90°) using Cu K_{α} radiation ($\lambda = 1.54184$ Å). An operating voltage of 30 kV and a current of 10 mA was kept constant for all the samples. The phase and the structural properties were investigated from the XRD data. The Rietveld refinement of the obtained XRD patterns of the samples was performed using FULLPROF software [15]. The lattice parameters were estimated from the refined crystallographic index files. The field emission scanning electron microscope (FESEM) of the samples was performed using a JEOL JSM-7610FPlus FESEM machine. From the FESEM images, the particle size, shape, and surface morphologies were studied in detail. Raman spectroscopy was performed using a HORIBA Scientific LabRAM HR evolution spectrometer (532-nm laser light source of power >300 mW). Ultraviolet-visible (UV-Vis) spectroscopy was performed to estimate the bandgap (E_g). A diffused reflectance spectrometer (Agilent Cary-60 UV-Vis) was used for this purpose.

Photoluminescence spectroscopy was performed to estimate the transitions within the bandgap using a Dongwoo Optron DM 500*i* spectrometer with a metal-vapor He-Cd laser source (excitation wavelength 325 nm). The Fourier transform infrared (FT-IR) spectroscopy of the samples were performed using the PerkinElmer Spectrum Two FT-IR spectrometer to determine the functional groups present and the vibrations of the functional groups present therein.

II. COMPUTATIONAL DETAILS

Spin-polarized DFT calculations were performed as implemented in the Vienna *ab initio* simulation package (VASP) [16,17]. The generalized gradient approximation–Perdew-Burke-Ernzerhof (PBE) [18] functionals with plane-augmented wave method was used for the description of electron-ion interactions in $SmVO_4$. The PBEsol [19] functional was used for the comparison of the geometrical parameters obtained within the PBE level of theory. An energy cutoff of 500 eV was used for the truncation of the plane-wave basis set and the representation of Kohn-Sham wave function with a smearing width of 0.01 eV for defining the electronic occupation. An energy convergence criterion of 10^{-6} eV was used throughout the calculations. A k-point grid of $8\times8\times8$ points was used to sample the Brillouin zone (BZ). A finite-difference-based method was used for the calculation of phonon dispersion along the BZ as implemented in the PHONOPY package [20]. A supercell of dimension $3\times3\times3$ was used for the calculation of the second-order force constants. A k-point mesh of $1\times1\times1$ is used to sample the BZ in reciprocal space. Nonanalytical term correction is added to the dynamical matrix to treat the long-range interaction of the macroscopic electric field in the phonon-dispersion. An energy cutoff of 800 eV was used during the phonon frequency calculation. The Born effective charges and static dielectric matrix was obtained from density functional perturbation theory. The calculation of second-order force constants involves a $3\times3\times3$ unit-cell throughout the present manuscript. Bilbao Crystallographic Server [21] was used to understand

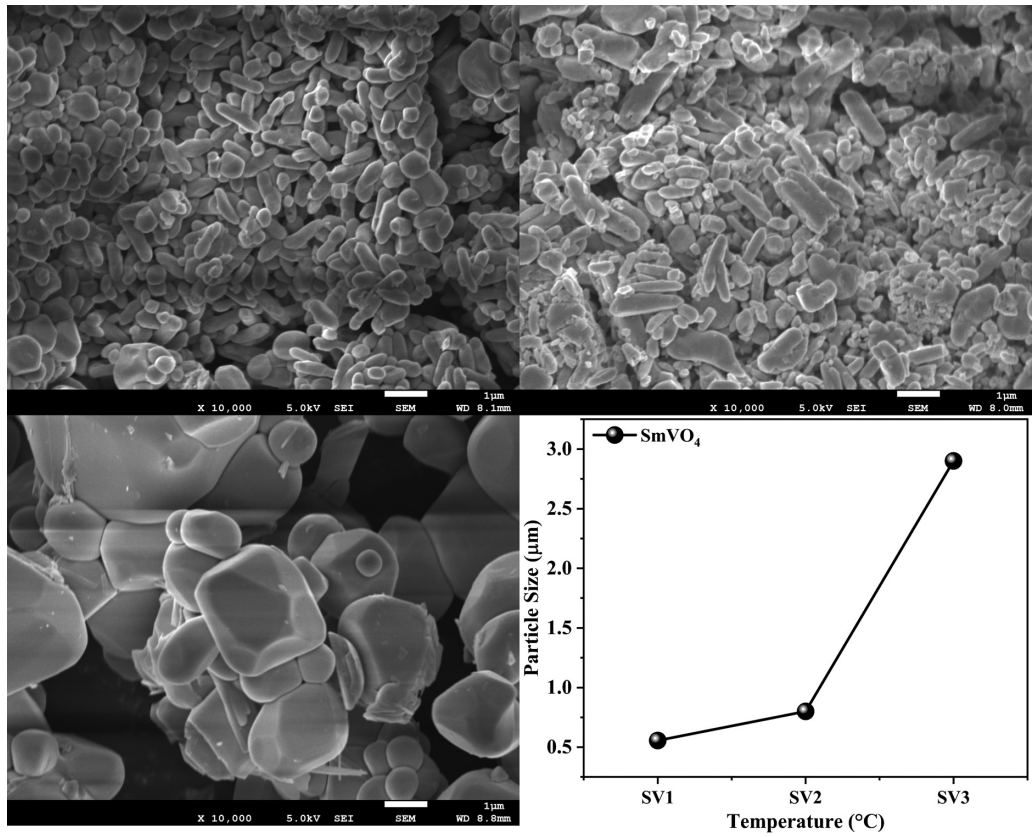

FIG. 1. FESEM images of SV1 (top left), SV2 (top right) and SV3 (bottom left) and graph showing the variation in grain size (bottom right).

the symmetry of IR and Raman modes. The interpolated IR spectra was produced by the methodologies adopted from a paper, based on the vibrational properties of tin chalcogenides [22]. The final electronic structure was obtained with the help of hybrid hybrid exchange-correlation functional (HSE06) [23–25]. Furthermore, a sampling mesh of $21\times21\times21$ points is used for describing the phonon interactions.

III. RESULTS AND DISCUSSIONS

A. Structural information on $SmVO_4$ (Samarium orthovanadate)

FESEM studies revealed a micrometer size of all samples (Fig. 1). Some morphological changes were observed with sintering temperatures for the three samples. For SV1, an elongated cylindrical shape was observed with an average

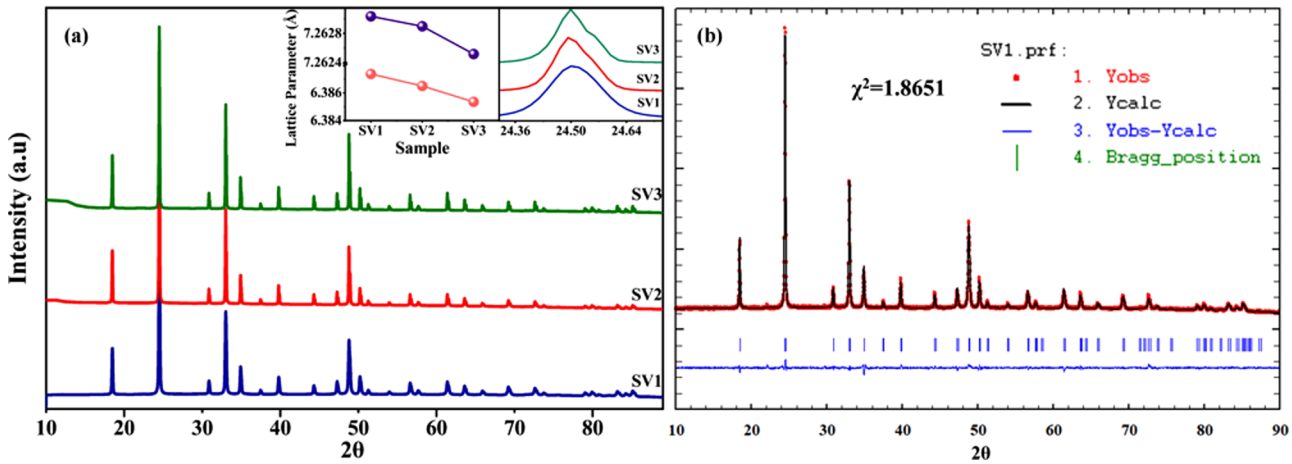

FIG. 2. (a) XRD pattern obtained for the samples. The first inset in (a) shows the variation in lattice parameters with temperature and the second inset in (a) shows variation of (200) peak with temperature. (b) The refinement data showing the experimental, calculated and difference profiles, and ticks indicating the positions of the Bragg reflections in the SV1 sample.

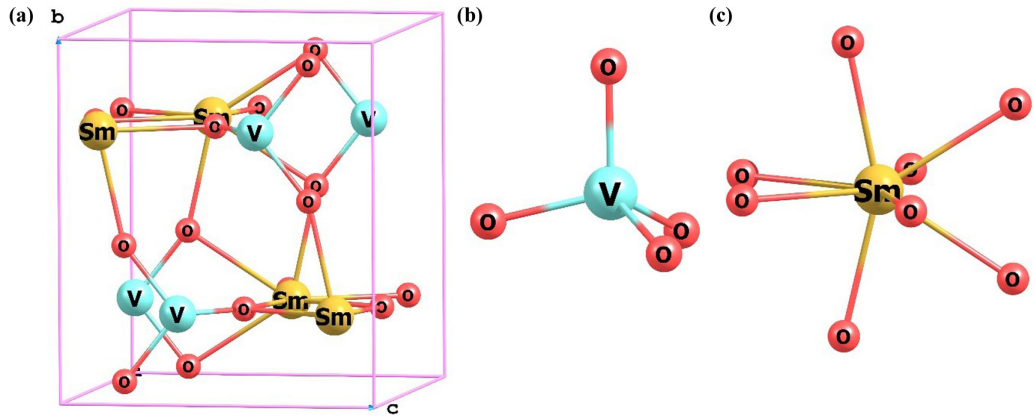

FIG. 3. (a) Tetragonal zircon unit-cell of $SmVO_4$, (b) the Vanadium tetrahedron surrounded by O atoms, and (c) Eight-coordinated Samarium atom.

length of ∼900 nm and a width of ∼200 nm. This nature gradually transformed into an almost elliptical shape for SV2 with an average grain size of ∼800 nm. Upon further heating, it was observed that the SV3 particles transform into a nearly cubical shape with an average grain size of ∼2000–3000 nm. The crystallinity of the particles seems to improve with increasing temperature from the morphological aspect. XRD patterns of the pure $SmVO_4$ has the tetragonal space group, $I4_1/amd$ with four formula units per unit cell having a point group of $4/mmm$ (or D_{4h}) (Fig. 2).

Concerning the space group settings, Sm atom is located on $4a$ (0, 3/4, 1/8), V atom located on $4b$ (0, 1/4, 3/8) and the O atom is located on $16h$ (0, y, z). The site-point groups for each Wyckoff position are as follows; Sm ($-42m$), V ($-42m$), and O (m) (Fig. 3). Here, the $SmVO_4$ is also represented as a triclinic primitive unit cell with two formula units per unit cell. Here, the DFT studies are used to discuss the IR and Raman properties of samarium orthovanadate at different temperature profiles. In the present work, three temperature profiles are considered at 873, 1023, and 1173 K. The widths of the peaks were seen to decrease with an increase in temperature. This is a clear indication of the increase in the crystalline size of the crystallites with sintering at higher temperatures. The intensity of the XRD data increased with the increase of sintering temperature, which is a clear indication of the improvement of the crystalline quality of the samples. Rietveld refinement was performed on the XRD data. The lattice parameters were observed to decrease with increasing temperature (Table I). The error in the lattice parameters (Fig. S1) and the Wyckoff positions of the individual atoms (Table S1) was obtained from the refinement data and provided in the Supplemental Material [26].

B. Bond length analysis

Geometrical parameters (such as bond lengths and bond angles) were acquired from the refined crystallographic information files for all the sintered structures using CCDC MERCURY software [27]. The geometrical parameters were calculated within the PBE and PBEsol level of theory. The calculated Sm-Sm bond length for SV1 is 3.96 Å, whereas the Sm-Sm bond length obtained from PBE (and PBEsol) level of theory is 4.00 Å (and 3.95 Å). The Sm-Sm bond length was found to remain constant across all temperature ranges. The geometrical parameters obtained from DFT-PBEsol level of theory suggest a more accurate picture of geometrical parameters [28]. Hence, these calculations were performed within the DFT-PBEsol level of theory. A similar trend in the Sm-V distance was also observed. However, a negligible increment was seen from SV2 to SV3. The structure, when observed from the c axis, was observed to have chains of alternate Sm and V atoms running parallel to the c axis forming a squarelike hollow structure, as seen in Fig. 4. A network of O atoms connects the Sm and V atoms of the same chain and the neighboring chains. As a result, the V atoms were observed to be forming VO_4^{3-} tetrahedral structures while the Sm forms perpendicular kitelike $SmVO_2$ structure with the next V atom parallel to the $|bc|$ and $|ac|$ planes. This also leads to the formation of Sm_2O_2 parallelograms formed parallel to the $|ac|$ and $|bc|$ planes similar to the case of the kites. As a result, the Sm is coordinated with eight O atoms, while the V is four coordinated. It was observed that these parallelograms and kites could be characterized by several Sm-O-Sm bonds expressed as β angles (Fig. 4). The angle O-Sm-O in the kites are represented as β_1, while in the parallelogram as β_2. β_1

TABLE I. Lattice parameters, the errors in the lattice parameters and the refinement parameters obtained from Rietveld refinement of the samples.

Sample	a	b	Error in a and b ($\times 10^{-4}$)	c	Error in c ($\times 10^{-4}$)	α	β	γ	χ^2	R_p	R_{wp}	R_{exp}
SV1	7.26303	7.26303	1.12	6.38736	1.03	90	90	90	1.86	15.7	10.1	7.41
SV2	7.26289	7.26289	0.76	6.38649	0.74	90	90	90	1.80	20.1	12.0	8.98
SV3	7.26252	7.26252	0.29	6.38534	0.46	90	90	90	1.80	23.2	12.9	9.59

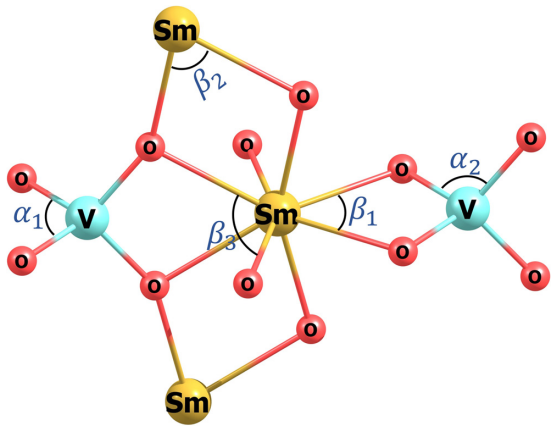

FIG. 4. Geometrical parameters of $SmVO_4$ expressed as α (O-V-O bond angles) and β (O-Sm-O bond angles).

increases with sintering temperature while β_2 decreases. The angle between two adjacent Sm-O bonds belonging to the kite and a parallelogram is expressed as β_3. With increasing sintering temperature, β_3 increases (Fig. 5). On the other hand, two of the O-V-O bond angles ~100°, called α_1, belong to the $SmVO_2$ kite structures. The other four angles are O-V-O bond angles ~115° in between neighboring kites. With sintering temperature, α_1 decreases while α_2 increases (Fig. 5).

C. Dynamic properties

The Born effective charge calculations are essential to determine polarizability (or polarization) of each individual species (M) to understand the vibrational properties of crystals (Table II). Here, the Born charges (Z^{*M}_{ij}) are described as induced polarization in the direction "i" (on the element M) due to unitary electric field along the direction "j". This is a tensor quantity, which is simplified by the crystal symmetries in a highly symmetric structure. Due to tetragonal symmetry of $SmVO_4$, only diagonal components (Z^{*M}_{11} and Z^{*M}_{33}) are of interest for Sm and V. However, due to the crystal symmetry, the nondiagonal elements ($Z^{*M}_{23} \neq Z^{*M}_{32}$) also play a vital role in governing the polarizability (and/or polarization) of oxygen atoms.

The atomic displacements around Sm create more polarization among the phonon modes. This might be due to the sharing of O p orbitals involved in the hybridization between Sm and V atoms. Such a large amount of Born charges on cation sites relates the strong dynamic coupling between phonon modes and displacement induced polarization.

The eigenvectors and their corresponding eigenvalues for $SmVO_4$ are shown in the Supplemental Material (Fig. S1) [26]. The modes depend upon their crystal symmetry and Wyckoff positions. The zircon structure of $SmVO_4$ consists of a primitive unit cell with 12 atoms (2Sm, 2V, 8O ~, i.e., two formula units) and corresponds to 36 ($3N$; N number of atoms) phonon modes for Γ point (0, 0, 0) symmetry. At the Γ point, the symmetry of all the 36 phonon modes are as follows; $\Gamma(D_{4h}) = [2A_{1g}+A_{2g}+A_{1u}+4A_{2u}+5B_{1g}+B_{2g}+2B_{2u}+5E_g+5E_u]$.

Here, E represents a doubly degenerate phonon mode, whereas A and B are nondegenerate phonon modes. The acoustic modes belong to the A_{2u} and E_u symmetries. So, the above representation is further decomposed and simplified as; $\Gamma_{\text{acoustic}} = A_{2u} + E_u$ and $\Gamma_{\text{optical}} = 2A_{1g} + A_{2g} + A_{1u} + 3A_{2u} + 5B_{1g} + B_{2g} + 2B_{2u} + 5E_g + 4E_u$. Finally, the atom-resolved phonon DOS for $SmVO_4$ was carefully analyzed (Fig. S3) [26]. The high-frequency phonon modes originate from the oscillations of the V-O bonds. From the phonon dispersion plot, the removal of degeneracy confirms the presence of E_u symmetry for acoustic modes. The E_u band readily splits into two sub-bands on moving along the $\Gamma \rightarrow M$ (or N) path in the reciprocal space. The numerical noises in the dynamical matrix were avoided by considering a larger cell (3×3×3) for the phonon calculations [29]. As shown in Fig. S3, all the phonon modes are positive throughout the BZ [26]. Also, all the phonon modes were found to be stable for all the samples under consideration throughout the BZ as shown in the Supplemental Material (Fig. S4) [26].

Using the quasiharmonic approximations, the decrease in lattice parameters under sintering temperature (experiment) was correlated with the thermal expansion coefficient (TEC). Considering the equilibrium geometry (~0 K), a volumetric expansion (and compression) is considered up to +5% (and −5%). For the calculation of heat capacity and thermal expansion, a free energy (H) vs volume (V)

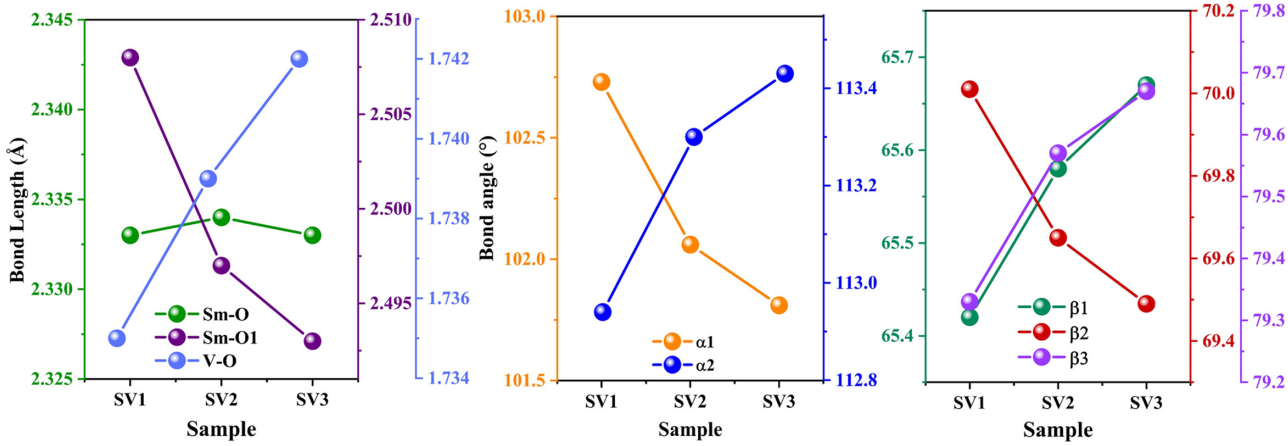

FIG. 5. Variation in the two types of Sm-O and V-O bond lengths and the bond angles with temperature.

TABLE II. Born charges (in units of e) for tetragonal $SmVO_4$ with different DFT functionals.

	Z^{*M}_{11}		Z^{*M}_{22}		Z^{*M}_{33}		Z^{*M}_{23}		Z^{*M}_{32}	
Species	PBE	PBEsol	PBE	PBEsol	PBE	PBEsol	PBE	PBEsol	PBE	PBEsol
Sm	4.231	4.237	–	–	5.098	5.048	–	–	–	–
V	3.119	3.142	–	–	4.530	4.582	–	–	–	–
O	−0.734	−0.726	−2.940	−2.964	−2.407	−2.407	1.169	1.165	1.164	1.156

plot was constructed at different temperature ranges. Initially, the C_p (heat capacity) was analyzed for $SmVO_4$ at different temperature ranges (from 10 to 1190 K, Fig. 6). After a certain temperature range (∼600 K), the heat capacity gradually becomes constant with a value of $C_{P,600K}$ = 279.91 J/K/mol to $C_{P,1190K}$=300.76 J/K/mol. From Dulong-Petit Law, the classical limit of C_P is expressed as C_P=3Rs (299.304 J/K/mol), where R is the gas constant and s (s=12) is the number of atoms per unit cell. The temperature-dependent heat capacity calculated for $SmVO_4$ matched with the classical limit of the heat capacity as suggested by the Dulong-Petit Law. Also, the calculated TEC shows a rapid increase with an increase in temperature and reaches a maximum value of 2.39 ($\times 10^{-5}$ K^{-1}) at 520 K. Beyond this temperature, there was a gradual decrease in the TEC up to 1.81 ($\times 10^{-5}$ K^{-1}) at 1190 K. The decrease in the value of thermal expansion with an increase in temperature beyond 520 K, suggests an increase in the invariance of the crystal structure [30]. The experimental lattice parameters and XRD patterns for $SmVO_4$ samples also suggest similar behavior with increasing sintering temperature. A phonon lifetime density plot was calculated for the ∼0 K (DFT) structure and SV1 structure with DFT methods. In Figs. 6(c) and 6(d), the lifetimes for acoustic modes (low-frequency

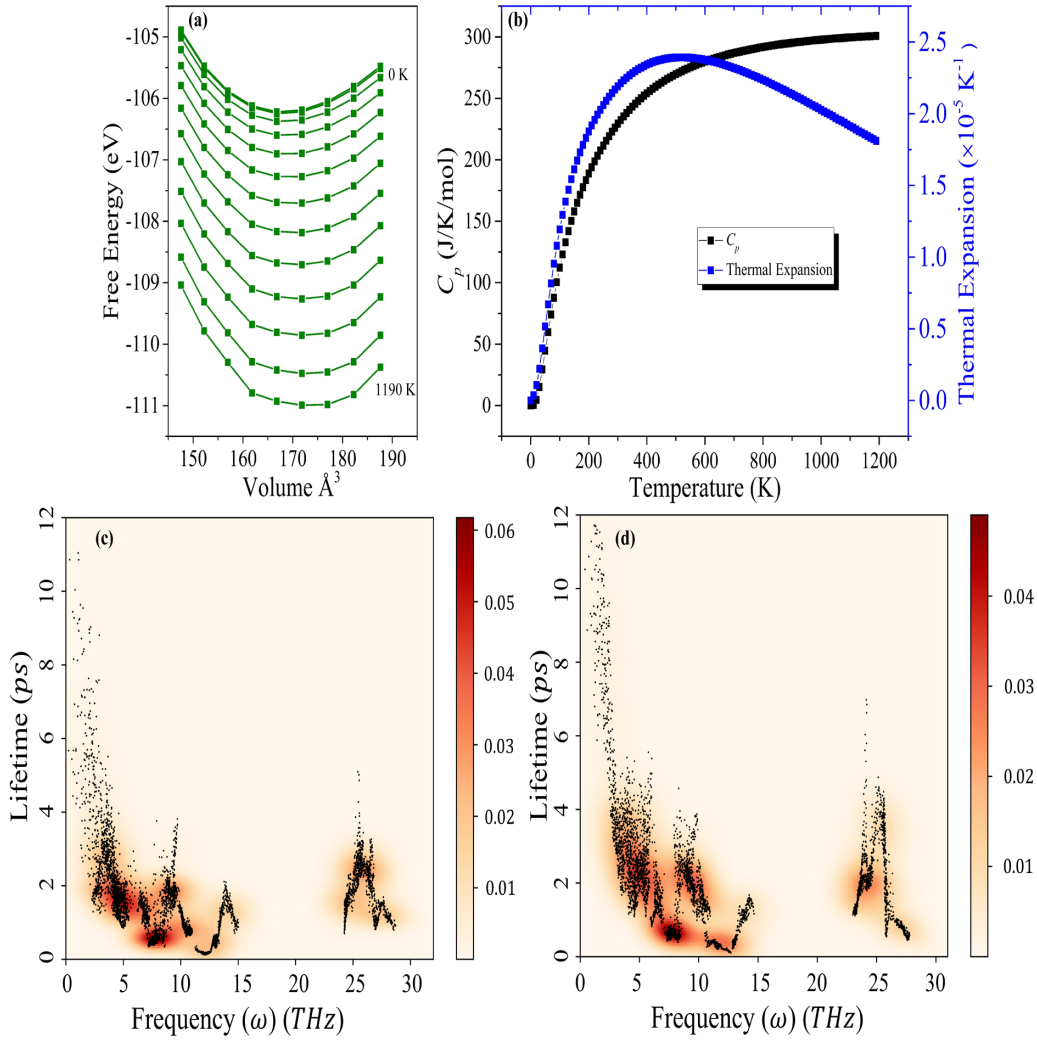

FIG. 6. (a) A free energy versus temperature plot, (b) A plot for thermal expansion and heat capacity (C_p) with temperature, (c) Phonon lifetime for ∼0 K structure, and (d) Phonon lifetime for SV1.

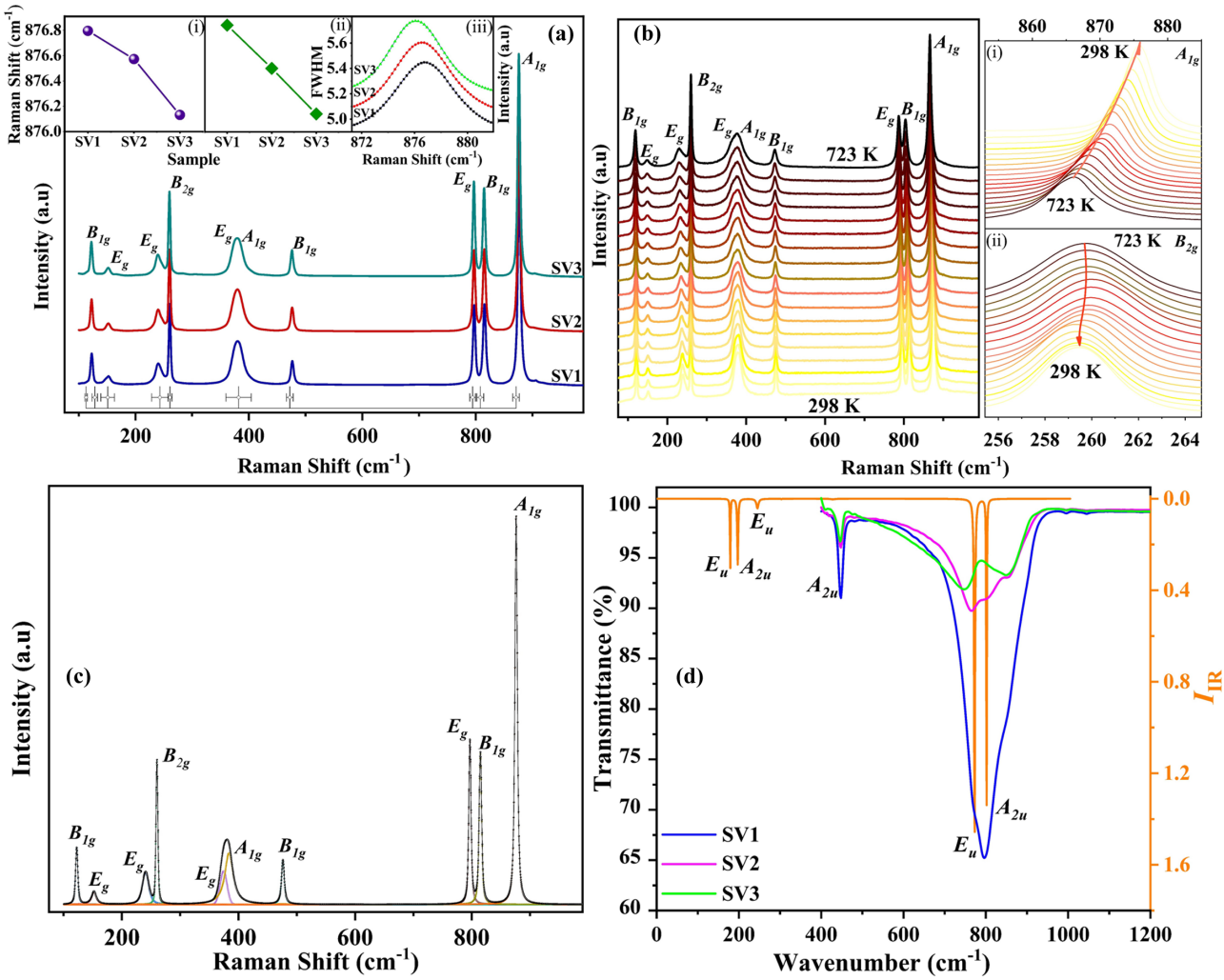

FIG. 7. (a) Raman spectra of the samples with sintering temperature. The first inset of (a) shows the Raman shift of the most intense A_{1g} mode, the second inset of (a) shows the variation in the FWHM of the A_{1g} mode, and the third inset of (a) shows the shift in the same A_{1g} mode. (b) Temperature-dependent Raman spectra of SV3. (c) Variation in peak parameters of the most intense A_{1g} with varying temperatures. (d) Variation in the B_{2g} in the temperature-dependent Raman spectra showing an opposing trend by blue shifting with increasing temperature. (e) Fitting showing all ten component modes of the SV3 Raman spectrum. (f) The experimental FTIR spectra for $SmVO_4$ samples projected along with the calculated IR spectra under DFT theory at room temperature (for SV1 at 300 K).

regime) is relatively larger compared to high-frequency modes (optical modes). A relatively larger phonon lifetime (∼2 to 4 ps) represents a smaller amount of anharmonicity (phonon-phonon coupling). Hence, the symmetry of phonon modes coupled to the crystal can be easily separable and visualized by other spectroscopic measurements such as Raman spectroscopy [31].

D. Raman and IR Spectra

As discussed above, at the Γ- point symmetry, the symmetry elements for Raman and IR modes can be described by the following irreducible representation; $\Gamma_{IR} = 3A_{2u} + 4E_u$ and $\Gamma_{Raman} = 2A_{1g} + 4\ B_{1g} + B_{2g} + 5E_g$. Hence, there are a total of seven IR active modes and 12 Raman active modes in $SmVO_4$ (Fig. 7). However, only ten out of the total twelve Raman modes were visible experimentally [Fig. 7(a)]. Some modes that are forbidden in a high-symmetry phase can be active in a distorted phase [32]. The degeneracy of these forbidden modes could be totally or partially removed in the distorted phase. Hence, the absence of the nondegeneracy of the degenerate phonon modes in this material explains the excellent strain-free crystallinity of the materials. The Raman modes which are experimentally observed are the following: $T(B_{1g})$, $T(E_g)$, $R(E_g)$, $\nu_2(B_{2g})$, $\nu_4(E_g)$, $\nu_2(A_{1g})$, $\nu_4(B_{1g})$, $\nu_3(E_g)$, $\nu_3(B_{1g})$ and $\nu_1(A_{1g})$.

For a better understanding of vibrational properties, all the eigenvectors are plotted in Fig. S1 with their corresponding symmetries of optimized structure. The Raman spectra of the $SmVO_4$ samples were in agreement with previous literature, both in the lower (100−480 cm^{-1}) and the higher (750−900 cm^{-1}) frequency ranges (Table III). The experimental Raman phonon modes were observed to redshift, as $SmVO_4$ was sintered from 873 to 1173 K. The A_{1g} (symmetric stretching) mode at ∼876 cm^{-1} is the most prominent peak of $SmVO_4$ Raman spectra, which belongs to the VO_4^{3-}

TABLE III. Temperature-dependent Raman modes with their corresponding symmetries.

Raman Mode Symmetry	Approximate theoretical Peak Position ωT (cm^{-1})	Observed Peak Position (SV1) ωE (cm^{-1})	Observed Peak Position (SV2) ωE (cm^{-1})	Observed Peak Position (SV3) ωE (cm^{-1})	FWHM (SV1)	FWHM (SV2)	FWHM (SV3)
$T(B_{1g})$	127.66	122.93	122.66	122.38	4.7686	4.7440	4.5479
$T(E_g)$	155.23	152.66	152.24	151.10	12.0730	11.8405	9.4451
$R(E_g)$	243.82	240.27	240.10	239.58	14.5440	14.1947	13.2750
$\nu_2(B_{2g})$	253.48	260.44	260.28	260.01	3.7194	3.7677	3.7716
$\nu_4(E_g)$	366.89	375.80	374.89	373.82	15.2807	13.9706	13.5598
$\nu_2(A_{1g})$	375.57	384.50	383.09	383.07	19.1257	20.3707	17.6780
$\nu_4(B_{1g})$	464.54	476.69	476.42	476.09	5.8960	6.2538	6.1388
$\nu_3(E_g)$	848.51	797.38	797.15	796.83	5.0677	5.01822	4.5470
$\nu_3(B_{1g})$	851.57	815.50	815.21	814.84	5.9947	5.6604	5.1650
$\nu_1(A_{1g})$	895.82	876.79	876.57	876.13	5.7408	5.4006	5.0412

tetrahedron. A shift and variation of the A_{1g} (~876 cm^{-1}) mode is observed with sintering temperature [Fig. 7(a)]. The E_g (ν_1 and ν_2) (848.51 cm^{-1}) symmetry belongs to the asymmetric stretching around the VO_4^{3-} units ($O_A-V_{I,II}-O_B$ and $\upsilon_2 = O_C-V_{I,II}-O_D$). The direction of movement between two VO_4^{3-} units were antisymmetric to each other along an axis ($V^{\uparrow}-V^{\downarrow}$ and $V^{\downarrow}-V^{\uparrow}$). E_g was observed at 786 cm^{-1} experimentally. The B_{1g} mode at 798 cm^{-1} belongs to the antisymmetric stretching (all the O atoms) within the V tetrahedron and antisymmetric movement of the tetrahedron towards each other [33–35]. A redshift, along with a decrease in full width at half maximum (FWHM), was observed experimentally with increasing sintering temperature. The reduction of lattice defects (nonstoichiometry, structural anomaly, etc.) can result in the sharpening of phonon modes [36,37]. Crystallinity is often linked with a sharper peak, also accompanied by a redshift [38–41]. The experimental structure (SV1) was simulated and compared with the DFT optimized structure to analyze such a redshift. All the phonon modes were calculated for SV1 with their corresponding symmetries. The simulated Raman spectra have been produced at 300 K for DFT optimized structure. There is a strong redshift observed on moving DFT optimized geometry from ~0 to 300 K (room temperature, RT). The calculated A_{1g} Raman mode shifts from 895.82 cm^{-1} (~0 K) to 875.80 cm^{-1}(RT). The calculated values match with the experimental observations. The softening (redshift) of the A_{1g} mode is directly associated with the lengthening of V-O bonds from 1.718 Å (~0 K) to 1.735 Å (RT). For all the phonon modes, similar redshifts in the $SmVO_4$ structure implies similar trends. With an increase in V-O bond length, the phonon frequency associated with symmetric stretching readily decreases. Lower values of phonon frequency involve a smaller amount of photon interaction energies.

Temperature-dependent Raman spectroscopy was performed on a pellet of SV3. The temperature range of the measurement was 298 to 723 K, with an incremental temperature step of 25 K [Fig. 7(b)]. All the Raman modes showed a redshift with increasing temperature except the B_{2g} mode at ~260 cm^{-1} which displayed a slight blueshift. All the modes appeared to broaden and become less intense with increasing temperature. However, after 523 K, the observed intensity showed fluctuations until 723 K. It was also observed that the E_g mode that had to be elucidated via fitting under ambient conditions [Fig. 7(e)] became easily detectable with increasing temperature. The Grüneisen parameter of each mode was calculated using the variation in the theoretical phonon frequency observed by varying the bulk modulus (Fig. 8). The equation $\gamma = (B_0/\omega_0)(d\omega/dP)$, was used to calculate the Grüneisen parameter of the individual modes. Here, ω_0 denotes the corresponding phonon frequency of each mode at ~0 K, while, the equilibrium bulk modulus, B_0 = 135.938 GPa. The B_{2g} mode at ~260 cm^{-1} has a negative Grüneisen parameter and the remaining modes displayed positive Grüneisen parameters (Table IV). Eigenvectors of the phonon modes gave a better insight into the reason for the blueshift observed in the B_{2g} mode and the redshifts observed in the rest of the modes. The atoms in the VO_4^{3-} tetrahedron units in the B_{2g} modes were seen to move in the same direction resulting in a very low effective displacement of the V ↔ O bonds. This results in a higher k value (force constant) indicating the strengthening of the bonds with increasing temperature in the B_{2g} mode. In other cases, such a bulk movement is absent, which gives rise to much higher effective displacements of the atoms with respect to their equilibrium positions. Therefore, a lower k value is observed, indicating a weakening of the bonds with higher temperatures (redshift).

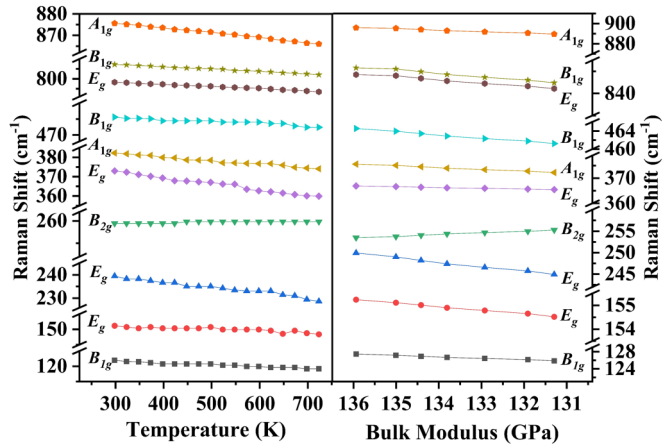

FIG. 8. Variation in phonon frequencies: (left) with temperature (experimental) and (right) with the bulk modulus (B) (theoretical).

TABLE IV. The calculated pressure coefficients ($d\omega/dp$) and Grüneisen parameter (γ) for $SmVO_4$.

Mode	ω_0 (cm^{-1})	$d\omega/dP$ (cm^{-1}/GPa)	Grüneisen parameter (γ)
B_{1g}	127.466	0.34074	0.36338
E_g	155.238	0.15227	0.13333
E_g	249.923	1.06646	0.58006
B_{2g}	253.483	−0.39141	−0.20990
E_g	366.892	0.31373	0.11624
A_{1g}	375.575	0.72052	0.26078
B_{1g}	464.547	0.70930	0.20755
E_g	848.511	1.42264	0.22791
B_{1g}	851.579	1.51809	0.24233
A_{1g}	895.823	1.40442	0.21311

A broad FT-IR spectrum was observed composed of at least three different vibrations in the ranges ∼450 and ∼720 − 860 cm^{-1} for all the three samples. A simulated IR spectrum was produced for $SmVO_4$ and compared with the corresponding experimental spectrum. The experimental and simulated spectra were consistent with each other, and other orthovanadates reported previously [42]. Theoretical calculations revealed two high-intensity modes belonging to the E_u and A_{2u} symmetries, matching with the broad experimental spectrum [Fig. 7(f)]. The E_u (υ_1 *and* υ_2) (doubly degenerate) symmetry belongs to the asymmetric ($\upsilon_1 = O_A{-}V_{I,II}{-}O_B$ and $\upsilon_2 = O_C{-}V_{I,II}{-}O_D$) stretching around the two VO_4^{3-} tetrahedron in a similar direction ($V_I^{\uparrow}{-}V_{II}^{\uparrow}$ and $V_I^{\downarrow}{-}V_{II}^{\downarrow}$; symmetrical movement along an axis). On the other hand, the A_{2u} mode belongs to the antisymmetric stretching of the VO_4^{3-} tetrahedron ($O_AO_B{-}V{-}O_CO_D$). The movements of both the tetrahedrons are symmetric to each other. The low intensity A_{2u} mode at ∼450 cm^{-1} represents the bending mode around the VO_4^{3-} tetrahedron. Theoretical calculations revealed all seven IR-active modes, as per group theory. However, the intensities are not equally probable for each individual transition and [Fig. 7(f)] all the high-intensity modes belong to the transition involving VO_4^{3-} tetrahedron. In Fig. 8, the changes in phonon frequencies ($d\omega$) with respect to temperature (experiment) and pressure (theoretical) are shown. The DFT simulated spectra showed a positive Grüneisen parameter for the all Raman modes with a lattice expansion (136 GPa → 131 GPa) in the $SmVO_4$ crystal (except B_{2g} mode). This softening is related to the volume contribution (or thermal expansion of the lattice). However, to account for the anharmonicity in the $SmVO_4$ phonon modes, a $d\omega/dT$ plot is also shown in Fig. 8 (left). Here, the dependence of ω on T under constant P represents the total anharmonicity in the $SmVO_4$ crystal. This softening of phonon modes (Fig. 8) is related to the three-phonon or four-phonon processes. They collectively describe the phonon-self energy in the $SmVO_4$ crystals as $\omega(T) = \omega_0 + \Delta\omega_{lat} + \Delta\omega_{anh}$ [43,44]. Here, $\Delta\omega_{lat}$ comes from thermal expansion (pure-volume) and $\Delta\omega_{anh}$ comes from pure-temperature contribution. The variation in the phonon frequencies of the individual Raman modes in the temperature dependent (experimental) and bulk modulus (theoretical) study have been compared and the relationship was consolidated from the Fig. 8 and Fig. S5 (Supplemental Material) [26].

E. Bandgap calculations

UV-Vis spectroscopy was performed to study the variation in band gap (E_g) and Urbach energy with temperature. Reflectance (R) was employed to calculate the absorption coefficient (α), availing the Kubelka-Munk function: $\alpha = \frac{(1-R)^2}{2R}$. The Tauc plot was used to calculate the direct and indirect bandgap, under the relation: $\alpha h\nu = A(h\nu - E_g)^n$, where; A is a constant, α is the absorption coefficient, $h\nu$ is the energy in eV and $n = 2$ and $(1/2)$ begets the indirect and direct bandgap, respectively [45]. The calculation of the direct bandgap yielded a trend where the bandgap reduces with increasing sintering temperature. A second transition at higher energy was observed for all three samples evincing a possible transition between two high-density bands. The direct bandgap calculations of the sample returned 3.75 eV for SV1, 3.74 eV for SV2, and 3.69 eV in SV3. From electronic

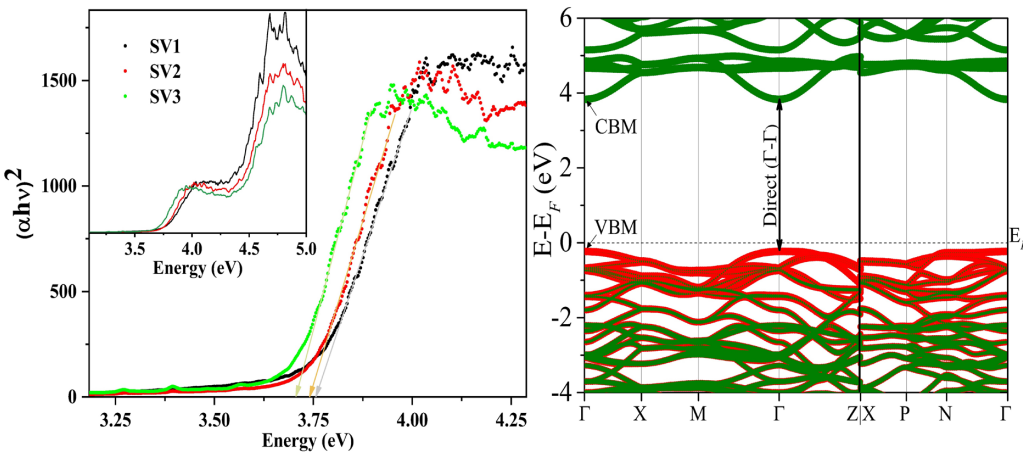

FIG. 9. The UV-Vis spectra of the samples, with the arrows showing an approximate value of the band gap. Atom-resolved band-structure for $SmVO_4$ with HSE06 level of theory. Here, the red color represents the O states, the green color represents the V states, and Fermi level (E_F) is set to 0 eV.

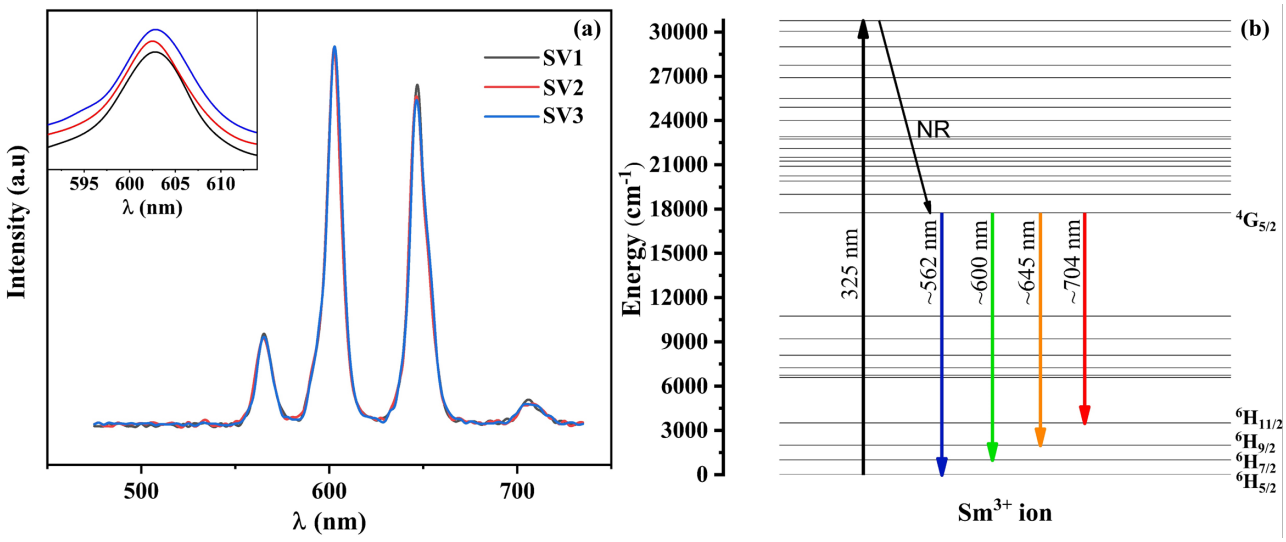

FIG. 10. (a) The photoluminescence spectra of the $SmVO_4$ samples. (b) Partial energy level diagram of along with radiative and nonradiative (NR) channels and energy transfer (ET) cross-relaxation (CR) channels.

structure calculations, a nonmagnetic insulating ground state is also observed with the help of DFT calculations (Fig. S6) [26]. Here, DFT calculations are employed to understand the nature of electronic transitions involved in the $SmVO_4$. The calculated bandgaps follow the same trend as the experimental findings. The calculated bandgaps from DFT (PBE)-level calculations were 2.63 eV (SV1), 2.61 eV (SV2) and 2.60 eV (SV3). As the PBEsol calculations underestimate the bandgaps compared to the experimental findings, HSE06 functionals were employed. The calculated bandgaps with HSE06 functionals were 4.06 eV (SV1), 4.03 eV (SV2) and 4.02 eV (SV3). An atom-resolved band-structure plot is also shown in Fig. 9. Here, the valence band maxima is majorly dominated by the O-states and conduction band minima dominated by the V states. A direct bandgap is observed, and transitions mainly occur between $\Gamma_{VB} \rightarrow \Gamma_{CB}$. The increase in the energy difference between the two transitions with increasing temperature can be corroborated using the electronic-structure calculations.

F. Photoluminescence Studies

Photoluminescence spectroscopy makes use of the principle of photoexcitation, which provides the energy necessary for the electrons in a material to excite to a higher energy level. The most preferred energy level can be found from the bandgap perceived from the UV-Vis spectrum. The energy of the emission bands is lower than the energy source used to cause excitation. In absorption, wavelength λ_0 corresponds to a transition from the ground vibrational level S_0 to the vibrational level of S_1, where S_1 corresponds to the energy level of wavelength λ_0. After absorption, the excited electron in the S_1 state without emitting any radiation de-excites to the lowest energy state of S_1 [Fig. 10].

The return to the S_0 state from the excited S_1 state results in the recombination of the excited electron with the hole created during excitation. However, this recombination can comprise of both radiative and nonradiative processes; the recombination rates administer the emission intensity of the different bands. Generally, the nonradiative transitions are considered the dominant recombination process. These are associated with impurities, the intensity of emission, and its dependence on the level of photoexcitation and temperature. The emission bands can be used to identify specific defects, while the emission intensity can be used to approximate the concentration of these individual defects. This assists in the study of impurities or dopants on the specific type of defect. Photoluminescence spectra had four distinct peaks as a result of the transition from the $^4G_{5/2}$ state to the $^6H_{5/2}$, $^6H_{7/2}$, $^6H_{9/2}$ and $^6H_{11/2}$ states (Fig. 10). This is consistent with previously reported data [46]. The most intense among these is the $^4G_{5/2} \rightarrow {}^6H_{7/2}$ (~600 nm = orange emission) transition. The $^4G_{5/2} \rightarrow {}^6H_{9/2}$ (645 nm ~ red emission) is almost comparable to the $^4G_{5/2} \rightarrow {}^6H_{7/2}$ transition. Other prominent peaks correspond to the $^4G_{5/2} \rightarrow {}^6H_{5/2}$ (~562 nm = green emission) and $^4G_{5/2} \rightarrow {}^6H_{11/2}$ (704 nm = red emission) transitions. These transitions have found application in high-density optical storage, color displays, undersea communication, and medical diagnostics [46].

IV. CONCLUSIONS

Sintering the $SmVO_4$ samples at higher temperatures results in the reduction of the lattice parameters. Rietveld refinement revealed variation in the bond lengths and bond angles with sintering temperature. This allowed a correlated study of the structural parameters, especially the bond length with the variations in the detected Raman modes. The data obtained from the DFT calculations confirmed the experimental vibrational modes: both the Raman and IR modes. All the Raman modes show a monotonous redshift with higher sintering temperatures. The temperature-dependent experimental Raman spectra study provided a more in-depth insight into the vibrational properties of the samples. The studies reveal a consistent redshift of all the modes except the B_{2g} mode for which a blueshift was observed. The theoretical calculations supported

such a trend. The behavior was further correlated with the bulk modulus when the Grüneisen parameter of only the B_{2g} mode was calculated to be negative, while all the other modes were positive. These trends are supportive of each other for all the modes. Similar to the Raman studies, the experimental IR modes were also supported by theoretical studies. Three experimental vibrational modes were observed that could be justified theoretically. Decreasing bandgap energy was observed with increasing sintering temperature. The trend was confirmed from theoretical calculations performed via standard DFT and HSE06 calculations. A characteristic spectrum of Sm^{3+} was revealed from photoluminescence studies. This luminescence can be used in high-density optical storage, color displays, undersea communication, and medical diagnostics.

ACKNOWLEDGMENTS

We thank the MEMS department for the FESEM facility and FTIR facility, the SIC IIT Indore for Raman equipment, and the photoluminescence facility. We also thank IIT Indore for the lab and computing facilities. S.K. thanks University Grant Commission for the fellowship.

[1] D. Errandonea, F. J. Manjón, A. Muñoz, P. Rodríguez-Hernández, V. Panchal, S. N. Achary, and A. K. Tyagi, J. Alloys Compd. **577**, 327 (2013).
[2] A. B. Garg, D. Errandonea, P. Rodríguez-Hernández, S. López-Moreno, A. Muñoz, and C. Popescu, J. Phys.: Condens. Matter **26**, 265402 (2014).
[3] T. Marqueño, V. Monteseguro, F. Cova, D. Errandonea, D. Santamaria-Perez, E. Bandiello, and M. Bettinelli, J. Phys.: Condens. Matter **31**, 235401 (2019).
[4] V. Panchal, D. Errandonea, F. J. Manjón, A. Muñoz, P. Rodríguez-Hernández, M. Bettinelli, S. N. Achary, and A. K. Tyagi, AIP Conf. Proc. **1665**, 030006 (2015).
[5] D. Errandonea, S. N. Achary, J. Pellicer-Porres, and A. K. Tyagi, Inorg. Chem. **52**, 5464 (2013).
[6] C.-T. Au and W.-D. Zhang, J. Chem. Soc. Faraday Trans. **93**, 1195 (1997).
[7] F. Chen, X.-L. Wang, S.-L. Li, G. Fu, K.-M. Wang, Q.-M. Lu, D.-Y. Shen, R. Nie, and H.-J. Ma, J. Appl. Phys. **94**, 4708 (2003).
[8] J. Liu, Q. Yao, and Y. Li, Appl. Phys. Lett. **88**, 173119 (2006).
[9] E. V Tsipis, M. V Patrakeev, V. V Kharton, N. P. Vyshatko, and J. R. Frade, J. Mater. Chem. **12**, 3738 (2002).
[10] Q. M. Le, T. H. Tran, T. H. Nguyen, T. K. Hoang, T. B. Nguyen, K. T. Do, K. A. Tran, D. H. Nguyen, T. L. Le, T. Q. Nguyen, M. D. Dang, N. A. Thu Nguyen, and V. M. Nguyen, Adv. Nat. Sci. Nanosci. Nanotechnol. **3**, 035003 (2012).
[11] C. Popescu, A. B. Garg, D. Errandonea, J.A. Sans, P. Rodriguez-Hernández, S. Radescu, A. Muñoz, S. N. Achary, and A. K. Tyagi, J. Phys.: Condens. Matter **28**, 035402 (2016).
[12] Q. Li, W. Zuo, and F. Li, Sci. World J. **2013**, 127816 (2013).
[13] F. Bosc, A. Ayral, P.-A. Albouy, and C. Guizard, Chem. Mater. **15**, 2463 (2003).
[14] A. Baszczuk, M. Jasiorski, and M. Winnicki, J. Therm. Spray Technol. **27**, 1551 (2018).
[15] J. Rodríguez-Carvajal, Phys. B **192**, 55 (1993).
[16] G. Kresse and J. Hafner, Phys. Rev. B **47**, 558 (1993).
[17] G. Kresse and J. Hafner, Phys. Rev. B **49**, 14251 (1994).
[18] J. P. Perdew, K. Burke, and M. Ernzerhof, Phys. Rev. Lett. **77**, 3865 (1996).
[19] G. I. Csonka, J. P. Perdew, A. Ruzsinszky, P. H. T. Philipsen, S. Lebègue, J. Paier, O. A. Vydrov, and J. G. Ángyán, Phys. Rev. B **79**, 155107 (2009).
[20] A. Togo and I. Tanaka, Scr. Mater. **108**, 1 (2015).
[21] E. Kroumova, M. I. Aroyo, J. M. Perez-Mato, A. Kirov, C. Capillas, S. Ivantchev, and H. Wondratschek, Phase Trans. **76**, 155 (2003).
[22] J. M. Skelton, L. A. Burton, A. J. Jackson, F. Oba, S. C. Parker, and A. Walsh, Phys. Chem. Chem. Phys. **19**, 12452 (2017).
[23] J. Heyd and G. E. Scuseria, J. Chem. Phys. **121**, 1187 (2004).
[24] J. Heyd, G. E. Scuseria, and M. Ernzerhof, J. Chem. Phys. **118**, 8207 (2003).
[25] A. V Krukau, O. A. Vydrov, A. F. Izmaylov, and G. E. Scuseria, J. Chem. Phys. **125**, 224106 (2006).
[26] See Supplemental Material at http://link.aps.org/supplemental/10.1103/PhysRevB.101.174112 for structural and dynamic properties.
[27] C. R. Groom, I. J. Bruno, M. P. Lightfoot, and S. C. Ward, Acta Crystallogr. Sect. B **72**, 171 (2016).
[28] G. M. Dongho Nguimdo and D. P. Joubert, Eur. Phys. J. B **88**, 113 (2015).
[29] S. Kumar, R. L. Kumawat, and B. Pathak, J. Phys. Chem. C **123**, 15717 (2019).
[30] V. Oddone, B. Boerner, and S. Reich, Sci. Technol. Adv. Mater. **18**, 180 (2017).
[31] A. M. A. Leguy, A. R. Goñi, J. M. Frost, J. Skelton, F. Brivio, X. Rodríguez-Martínez, O. J. Weber, A. Pallipurath, M. I. Alonso, M. Campoy-Quiles, M. T. Weller, J. Nelson, A. Walsh, and P. R. F. Barnes, Phys. Chem. Chem. Phys. **18**, 27051 (2016).
[32] M. N. Iliev, M. V. Abrashev, J. Laverdière, S. Jandl, M. M. Gospodinov, Y. Q. Wang, and Y. Y Sun, Phys. Rev. B **73**, 064302 (2006).
[33] I. E. Wachs, Catal. Today **27**, 437 (1996).
[34] L. Abello, E. Husson, Y. Repelin, and G. Lucazeau, Spectrochim. Acta Part A Mol. Spectrosc. **39**, 641 (1983).
[35] T. R. Gilson, O. F. Bizri, and N. Cheetham, J. Chem. Soc. Dalton Trans. **3**, 291 (1973).
[36] J. W. Ager, D. K. Veirs, and G. M. Rosenblatt, Phys. Rev. B **43**, 6491 (1991).
[37] B. Li, D. Yu, and S.-L. Zhang, Phys. Rev. B **59**, 1645 (1999).
[38] R. J. Nemanich, S. A. Solin, and R. M. Martin, Phys. Rev. B **23**, 6348 (1981).
[39] W. H. Weber, K. C. Hass, and J. R. McBride, Phys. Rev. B **48**, 178 (1993).

[40] F. Tuinstra and J. L. Koenig, J. Chem. Phys. **53**, 1126 (1970).
[41] G. Gouadec and P. Colomban, Prog. Cryst. Growth Charact. Mater. **53**, 1 (2007).
[42] W. Chen, L. Q. Mai, J. F. Peng, Q. Xu, and Q. Y. Zhu, J. Mater. Sci. **39**, 2625 (2004).
[43] H. Tang and I. P. Herman, Phys. Rev. B **43**, 2299 (1991).
[44] S. Dogra Pandey, J. Singh, K. Samanta, N. Dilawar Sharma, and A. K. Bandyopadhyay, J. Nanomater. **2015**, 492967 (2015).
[45] Y. Huang, L. Luo, J. Wang, Q. Zuo, Y. Yao, and W. Li, J. Appl. Phys. **118**, 044101 (2015).
[46] C. Basavapoornima and C. K. Jayasankar, J. Lumin. **153**, 233 (2014).